References

[1] J. Galindo, A. Gil, R. Navarro, D. Tarí, Analysis of the impact of the geometry on the performance of an automotive centrifugal compressor using CFD simulations, Applied Thermal Engineering 148 (2019) 1324 – 1333. doi:10.1016/j.applthermaleng.2018.12.018.

Analysis of the impact of the geometry on the performance of an automotive centrifugal compressor using CFD simulations

J. Galindo[a], A. Gil[a], R. Navarro[a], D. Tarí[a,*]

[a] *CMT - Motores Térmicos, Universitat Politècnica de València*
Camino de Vera, 46022 Valencia

Abstract

During the latest years, downsizing in internal combustion engines has moved the operating conditions of the compressor closer the surge limit. Surge onset depends on the geometry of the compressor inlet and is difficult to predict. Unfortunately, the determination of the surge line is essential for engine design and calibration, since surge is an oscillating phenomenon that endangers the turbocharger integrity. This work is addressed to study the impact of placing different geometries, namely a tapered duct, a convergent-divergent nozzle and a divergent nozzle in the compressor inlet on different compressor parameters such as stability, efficiency and noise emission. 3D-CFD simulations are performed using the commercial code STAR-CCM+ at both near-surge conditions and high mass flow rate, focusing on the flow structures generated by each configuration. The results are compared with corresponding experimental tests and show a meaningful sensitivity of geometry to the performance, indicating potential benefits of using some of these geometries in turbocharger configurations.

Keywords: Centrifugal turbocharger, Computational Fluid Dynamics, Surge, Compressor performance, Noise emission

*Corresponding author. Tel.: +34 963 877 650

Email addresses: galindo@mot.upv.es (J. Galindo), angime@mot.upv.es (A. Gil), ronagar1@mot.upv.es (R. Navarro), datade@mot.upv.es (D. Tarí)

1. Introduction

In the recent years, internal combustion engines have evolved due to the technological development usually driven by steady restriction on pollutant emissions [1, 2]. A technique that introduces an enhancement in both pollutant emission reduction and increased performance is the turbocharging of the engines [3, 4]. The increase in flow density and specific power is employed to reduce the engine size (spread trend known as *downsizing*), boosting the request of low-end torque [5]. In order to achieve stable conditions at the compressor when lowering the requested mass flow rate, the operating limit (surge) needs to be clearly defined, being as low as possible. When the compressor operating point crosses this limit, often during transient evolutions [6], undesirable phenomena appear, such as violent axial oscillations of the compressor wheel, drop in compression rate, oil leaks, turbocharger damage [7], etc.

Considering this, great effort has been made developing different techniques that allow avoiding an early entrance of the operating point into the surge. There are active control techniques that vary a reservoir volume upstream or downstream of the compressor, canceling the pulsations generated by the surge phenomenon [8]. According to Zhang and Zheng [9], the piping design of the intake system can be tuned to neutralize the distortions that appear, slightly increasing the efficiency peak. Some authors observed an increase of the surge margin by placing different geometries at the compressor inlet [10, 11, 12]. Desantes el al. [13] studied how the compressor map was shifted towards lower mass flow rates by placing a Convergent-Divergent (C-D) nozzle very close to the inducer. Sharma et al. [14], Minyang et al. [15] and Semlitsch and Mihăescu [16] studied the influence of using bleed slots, technique also known as ported shroud or casing treatment. Galindo et al. [10] and Tomita et al. [17] used a pre-whirl or IGV device to modify the incidence of the flow at the inducer, improving the compressor map. The impact of using realistic inlet geometries has also been studied by different authors [18, 19].

Nevertheless, each configuration, in addition of introducing a benefit in the surge margin, may have a positive or negative impact on other compressor global variables. The efficiency and compression ratio are often linked with the pressure loss introduced by a given geometry. On the other hand, the characteristiques of the emitted noise depend on several aspects, both geometrical [20, 21] and operational ones [22, 23].

Although the impact of each geometry can be assessed by comparing compressor experimental measurements (i.e., efficiency, compression ratio and noise emission [24]), only a better understanding of the flow behavior allow researchers to extract design guidelines. Due to the complex geometry of the compressor and packaging constraints, it is hard to perform non-intrusive flow measurements near the compressor mouth, neither it is possible to have local measurements along the impeller passages. Experimental measurements can be made with, for example, optical techniques such as LDV or PIV [25]. However, in order to have a complete solution of the flow field, CFD calculations provide results that have proven to be meaningful in the past for studying other compressor inlet geometries [26] and noise emissions [27, 28].

In this work, the influence of different promising compressor inlet geometries in its performance is analyzed using the 3D-CFD software StarCCM+[29], allowing a fundamental analysis of the flow structures that appear within each configuration. In Section 2, the geometries selected are introduced and described. The methodology and the numerical setup is noted in Section 3. The discussion of the results is written in Section 4 and finally, the concluding remarks are shown in Section 5.

2. Selection of geometries

The geometries selected for this work are inspired on the ones that have been experimentally analyzed by Galindo et al. in a previous study [24]. Steady and transient measurements were made in that work using an engine test bench in order to simulate real pulsating conditions. A straight duct will be used as the reference case. This geometry is shown in Fig. 1a with the impeller on the bottom part.

The first of the proposed geometries is the tapered duct. It is created by reducing the inlet duct diameter approximately from 2 times to 1 time the impeller diameter in the direction of the incoming flow. Previous studies [30], found a surge margin increase when using this intake of about 20%. A detailed view of this geometry is shown in Fig. 1b.

The next intake line is composed by a nozzle with a convergent part that reaches a throat and then a divergent part that recovers the upstream diameter and discharges close to the inducer. The potential benefits of this geometry were described by Desantes et al. [13] in a study where a surge margin improvement of 30% and a slight efficiency rise was observed on the whole compressor map. Alas, at high mass flow rates a worsening of the

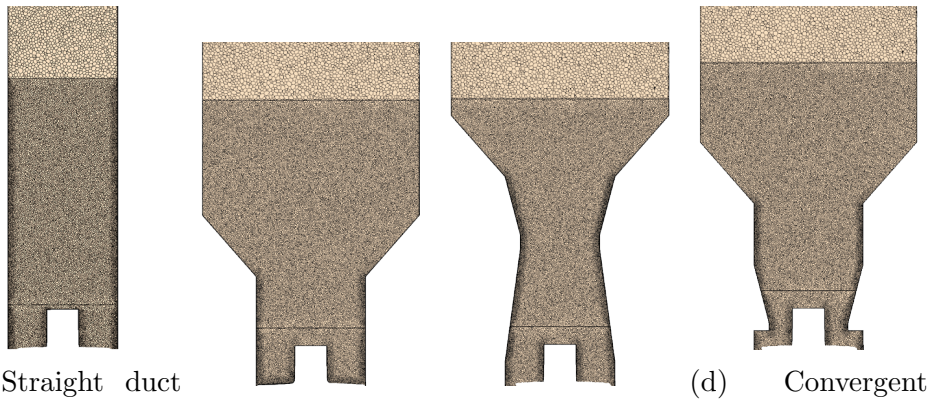

(a) Straight duct (baseline) (b) Tapered duct (c) C-D nozzle (d) Convergent nozzle

Figure 1: Inlet geometries outline and cross-section of mesh.

compressor performance appeared. A section of the Convergent-Divergent (C-D) nozzle designed for this work can be seen in Fig. 1c.

Finally, the previous configuration is modified by removing the divergent part from the throat, so that it discharges directly on the inducer. The inlet section is apparently reduced, virtually modifying the trim of the compressor and greatly affecting on its performance. In Fig. 1d is depicted a detailed view of this convergent nozzle.

The 3D model of the compressor used in this work and the compressor used by Galindo et al. [24] in the aforementioned experimental work are much alike (same number of blades and splitters, similar trim...), which allows a comparison between results to analyze the consistency of the trends. A slight difference in impeller diameter is corrected scaling the inlet geometries accordingly.

3. CFD setup and methodology

Broatch et al. [22, 27] proposed a numerical setup and validated it through an experimental assessment using a continuous flow turbocharger test cell. The validation covered global variables (thermal efficiency, compression ratio) and acoustic emission. An analogous numerical setup is selected for the current work. Considering that the geometry of the compressor and the operating conditions employed in this work are also similar to the ones used by Broatch et al. [22, 27], an equivalent validity of the predicted results is expected.

Concerning the numerical domain, all the cases share the housing, the rotor, the volute and the outlet duct, differing only in their specific inlet geometry. In Fig. 2 is depicted a close-up view of the geometry and the mesh of the compressor wheel. It can be appreciated that the full 360°-resolved rotor is considered, including the tip clearance between the blade tips and the housing in CAD-like conditions, since Galindo et al. [31] proved that the actual tip profile in working conditions does not affect noise prediction and only increases slightly pressure ratio and compressor efficiency. The mesh settings were previously used by Navarro [32] for a similar compressor showing grid independence. The complete mesh is composed by about 10 million polyhedral cells, distributed among the different regions as seen in Table 1. The wall resolution is increased by reducing the cell size and adding prism layers, producing y^+ values below 5 on the surfaces, thus assuring these cells are in the viscous sub-layer zone and properly solving the flow [28]. For a better solution of the flow structures in the inlet ducts near the impeller, a finer meshing is applied in these areas, specifically two inducer diameters upstream from the inducer planes, a distance in which backflows are expected to be confined [22], as can be observed in Figure 1.

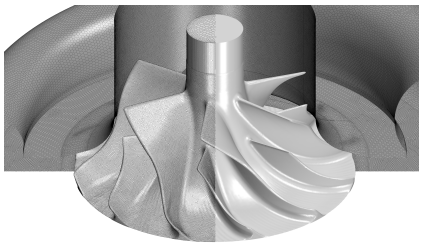

Figure 2: Rotor geometry and mesh.

Region	**Cells (M)**	**Intake**	**Cells (M)**
Rotor	4.1	Straight	1.9
Diff.,volute	1.6	Tapered	4.3
Outlet	0.7	C-D nozzle	3.9
Intake	1.9-4.4	Conv. nozzle	4.4

Table 1: Millions of cells in each region, distinguishing between intake geometries.

Regarding the numerical setup, the StarCCM+ [29] segregated flow solver with ideal gas properties for the air is employed. The turbulent approach is

addressed using Detached Eddy Simulation, with $k-\omega$ SST submodel "which functions as a sub-grid-scale model in regions where the grid density is fine enough for a large-eddy simulation, and as a Reynolds-averaged model in regions where it is not" [33]. Several researchers [34, 35, 36] have satisfactorily used this same approach with similar compressor simulations. The problem is solved using a 2^{nd} order transient solver, with a time step equivalent to a compressor wheel spin of 4°. This time-step size allows a proper prediction of noise emission in plane wave range, enough to allow the proposed noise assessment [32].

Due to the high computational effort that each simulation implies, it is decided to analyze two operating conditions per geometry along the 160 krpm isospeed line, one point at 30 g/s close to the surge line to study the flow structures that appear at these conditions, and one at operating point at 100 g/s to determine the impact of the inlet geometries on the global variables of the compressor. Additionally to the mass flow rate, it is imposed the compressor outlet pressure at 2 bar and the compressor speed at 160 krpm.

Once the relevant signals have reached periodicity (after ≈100 compressor rotations), the simulation is run for 130 additional rotations at least to record time history of variables. Time-averaged values of pressure, temperature and velocity at the whole domain can be then obtained for post processing, creating scalar scenes as well as global variables, namely the compressor efficiency and the compression ratio, defined in Equations 1 and 2 respectively.

$$\Pi_{t,t} = \frac{p_{out,t}}{p_{in,t}} \tag{1}$$

$$\eta_s = \frac{\dot{W}_s}{\dot{W}} = \frac{T_{in,t}\left(c_{p,in}\ \Pi_{t,t}^{\frac{\gamma-1}{\gamma}} - c_{p,in}\right)}{c_{p,out}\ T_{out,t} - c_{p,in}\ T_{in,t}} \tag{2}$$

Concerning the noise emission analysis, surface average monitors are set in two cross-sections close both to inlet and outlet corresponding boundaries. Then, using the Method of Characteristics (MoC) as defined in Eq. 3 [37], the forward and backward pressure waves are obtained.

$$p_{forw} = p_{ref}\left[\frac{1}{2}\left(1+\left(\frac{p}{p_{ref}}\right)^{\frac{\gamma-1}{2\gamma}}\left(1+\frac{\gamma-1}{2}M\right)\right)\right]^{\frac{2\gamma}{\gamma-1}} \tag{3}$$

$$p_{back} = p_{ref}\left[\frac{1}{2}\left(1+\left(\frac{p}{p_{ref}}\right)^{\frac{\gamma-1}{2\gamma}}\left(1-\frac{\gamma-1}{2}M\right)\right)\right]^{\frac{2\gamma}{\gamma-1}}$$

Broatch et al. [27] showed that these MoC-decomposed pressure signals obtained at cross-section were comparable to that measured experimentally at plane-wave range. According to Eriksson [38], the threshold of this range is set by the onset of the first asymmetric mode, which occurs at a frequency of:

$$f_{c,a} = 1.84\frac{a}{\pi D}(1-M^2)^{1/2}. \tag{4}$$

This expression predicts the onset of the asymmetric modes at 3.8 kHz and 6 kHz for inlet and outlet ducts, respectively. The Power Spectral Density (PSD) of these pressure traces is calculated using Welch's overlapped segmented averaged [39] approach. The Hamming function is selected for defining the window length of the blocks, setting the frequency resolution in 150 Hz for inlet and outlet PSD at both operating points. Additionally, the sound intensity is calculated using equation 5, according to Holland and Davies [40]. A frequency range from 300 Hz to the corresponding first asymmetric mode onset frequencies is considered for computing the Sound Intensity Level (SIL). Low-end frequencies are not taken into account for the calculation of this parameter due to their reduced impact on the human subjective noise perception. A reference sound intensity of 10^{-12} W/m^2 is used the SIL calculation (Eq. 6).

$$\begin{aligned} I &= I_{forw} - I_{back} \\ &= \frac{1}{\rho_0 a_0}\left(|\hat{p}_{forw}|^2(1+M)^2 - |\hat{p}_{back}|^2(1-M)^2\right) \quad \frac{W}{m^2} \end{aligned} \tag{5}$$

$$SIL = 10\ \log_{10}\left(\frac{\sum_{f=500Hz}^{5000Hz} I(f)}{10^{-12}}\right) \quad (dB) \tag{6}$$

4. Results and discussion

The experimental tests conducted by Galindo et al. [24] showed an advantageous influence on the compressor parameters for all the proposed configurations against the baseline straight duct, highlighting the increased surge margin. A qualitative summary of the surge margin improvements found in different researches is shown in Table 2. Each plus sign (+) represents a surge improvement of 10%.

Auth./Geom.	**Tap. duct**	**C-D Nozzle**	**C. Nozzle**
Galindo et al. [41]	++		
Desantes et al. [13]		+++	
Galindo et al. [24]	+	+	++

Table 2: Summary table of the impact of different inlet geometries from different studies on the compressor surge margin.

In the case of the tapered duct and the C-D nozzle, the compression ratio at high mass flow rates was kept without detriment and the efficiency was also kept or slightly increased with the C-D nozzle through all the compressor map. Conversely, the convergent nozzle showed an efficiency decrease and worse compression ratio at high mass flow rates but lower noise emission, both phenomena possibly caused by the cross-section restriction of the throat.

It would be desirable to find the actual surge limit of each configuration at a given compressor speed, however with the current methodology it would require an excessive computational effort. Instead, this work is mainly devoted to the phenomena involved with the inception of surge appearance, studying, as aforementioned, different quantitative and qualitative parameters that may point out the closeness of this stability limit. However, to analyze the behavior of the compressor at other operating conditions, in section 4.2 the compressor performance is assessed as well at same compressor speed but much greater mass flow rate.

4.1. Points of low mass flow rate

Focusing the attention on the low mass flow rate operating points, Fig. 3 depicts the streamlines upstream the compressor for different intake geometries. Streamlines in blue represent the downstream flow coming from the inlet boundary and red streamlines highlight the backflow that is being recirculated from the inducer plane of the compressor.

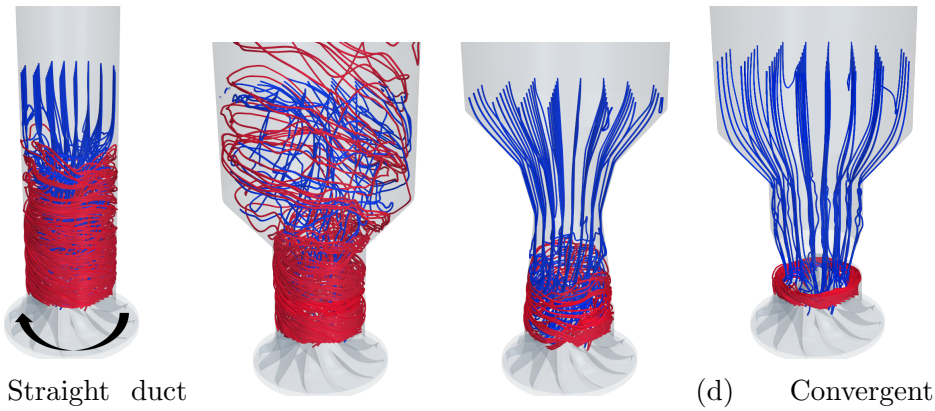

(a) Straight duct (baseline) (b) Tapered duct (c) C-D nozzle (d) Convergent nozzle

Figure 3: Inlet (blue) and recirculated (red) streamlines for the different inlet geometries at low mass flow rate.

As can be seen in Fig. 3, each configuration produces a different recirculation pattern. In the reference straight duct, the recirculation reaches about two inducer diameters upstream of the wheel, but for the C-D nozzle, this region is contained in the divergent part, with a length of about an inducer diameter. With the convergent nozzle, the recirculation is only produced within the free space between the throat and the wheel. Conversely, the tapered geometry offers a sudden increase of the diameter to the backflows that travel upstream, where lower inlet velocities are found, reducing the momentum and swirl transmission between both flows and causing a recirculation region larger than five inducer diameters. It is worth mentioning that this recirculation phenomenon appears at low mass flow rates, positively impacting on the stability of the compressor [42]. It generates a rise of the incoming mass flow rate and thus, an increase in momentum. In addition, the available cross-section the flow has to enter through the inducer plane is reduced, implying a further rise in velocity and momentum.

Using the time-averaged flow parameters at the inducer plane, the incoming and outgoing (recirculation) mass flow rates and the incoming momentum relative to the momentum of the straight configuration are calculated. In Table 3 a quantitative evaluation of these indicators is provided.

Compared with the reference configuration, the results show that higher recirculation mass flow rates are obtained with the tapered duct and lower with the nozzles. Although this is consistent with the length of the recir-

	Str.	**Tap.**	**CD-N**	**C-N**
Upstream (g/s)	8.2	8.5	7.0	6.3
Downstream (g/s)	38.2	38.5	37.0	36.3
Momentum (%)	100	100.87	91.82	91.48

Table 3: Recirculated mass flow ratios at low mass flow rate.

culations, it does not imply a direct correlation with the improvements of surge margin obtained on the experimental tests carried out by Galindo et al. [24]. A similar reasoning can be drawn from the incoming momentum results. Thus, in spite of being interesting indicators of the state of the flow at the compressor inlet, these parameters cannot be directly used to predict the surge appearance.

As can be observed in Fig. 3, due to the rotation of the wheel, the tangential velocity of the recirculated flow is high and has a swirl component that is transferred to the incoming flow as it is redirected towards the compressor [42], acting like a pre-swirl device and increasing the pre-rotation of the flow [10, 16, 17]. Notice that the incoming flow presents an increase of angular momentum caused by the recirculation, which rotates in the same direction as the compressor wheel (see arrow in Fig. 3). The increase of axial momentum and reduction of incidence angle due to those backflows delay onset of surge.

Other parameters that can be extracted from the state of the flow at the compressor inducer are the angles of the velocity triangle of the compressor inducer, defined in Fig 4. Using a cylindrical coordinate system, the axial and tangential time-averaged components of the velocity are considered in an annulus-shape region in the inducer plane. The annulus is defined between the spans 0.3 and 0.7 of the impeller passage, representing a characteristic incoming flow region (the recirculation area is skipped, as well as the area very close to the hub). The inducer plane is moved an offset of 2 mm upstream of the leading edge, avoiding the perturbations of the leading edges on the averaged velocity components. Additionally, between the aforementioned spans where the annulus is defined, the blade angle at the leading edge ($\beta_{l.e.}$) is also averaged. Then, using equations 7, 8 and 9, α and β angles and the incidence are respectively obtained.

$$\tan \alpha = \frac{c_u}{c_a} \tag{7}$$

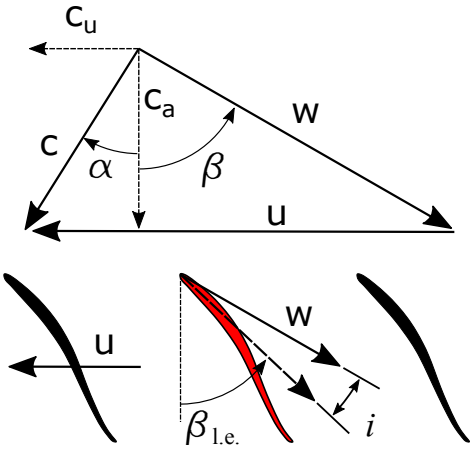

Figure 4: Velocity triangle at the compressor inducer plane.

$$\tan\beta = \frac{c_u - u}{c_a} = \frac{c_u - \omega\ r}{c_a} = \frac{c_u - N(rpm)\frac{2\pi}{60}\ r}{c_a} \tag{8}$$

$$Incidence = \beta - \beta_{l.e.} \tag{9}$$

The results of the velocity triangle angles and incidence for the low mass flow rate operating points are shown in Table 4.

Angle [°]	**Str.**	**Tap.**	**CD-N**	**C-N**
α	36.8	36.9	39.6	45.1
β	55.6	56.0	57.0	54.4
i	8.6	9.0	10.0	7.4

Table 4: α and β angles and incidence at low mass flow rate.

The first feature that outstands when analyzing Table 4 is the non-null values of the α terms for all cases, even though there are no pre-swirling devices mounted on the compressor inlet. This is only explained by a swirl transmission of the recirculated flow to the incoming stream. This mechanism is produced due to the rotation of the wheel, which sets a high tangential component of the flow that exits the inducer in an upward direction. Then, depending on different factors, such as the available recirculation region, the recirculated mass flow rate and the outgoing swirl, the transmission of swirl may vary and a different alpha angle will be produced. On the other side,

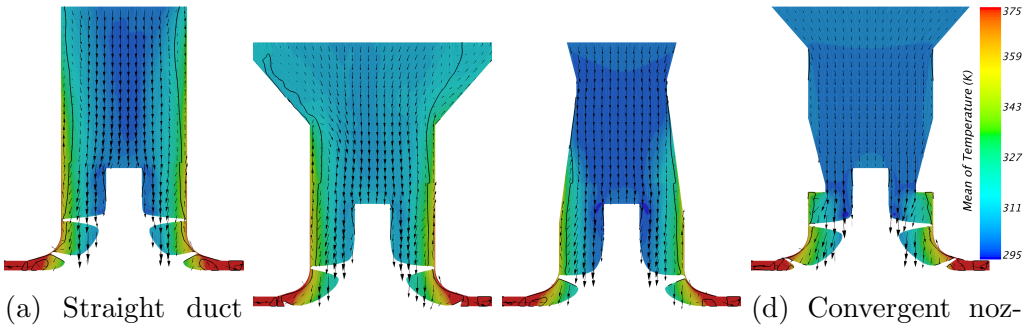

(a) Straight duct (baseline) (b) Tapered duct (c) C-D nozzle (d) Convergent nozzle

Figure 5: Axial section of linear integral convolution of mean velocity, scalar of mean temperature, mean velocity vectors and black solid line indicates null axial velocity for the low mass flow rates simulations.

the beta angle depends on the alpha angle, the speed of the compressor wheel (which is constant in this case for all the configurations), and the axial component of the incoming flow. It is worth mentioning that a higher recirculation imply higher axial velocities, which affects these angles (see Table 3).

Analyzing the results obtained for the simulations of low mass flow rates displayed in Table 4, it is observed that a similar velocity triangle is obtained with the straight and tapered ducts. This is consistent with the results obtained in Table 3, where similar values of backflows were obtained with these two intake geometries. Conversely, with both nozzles is obtained a higher α angle, implying that more swirl transfer is being produced. However, the lower recirculation of the C-D nozzle produce a higher incoming area and lower axial average velocities on the annular section where the angles are calculated, producing a slightly higher β angle and incidence. Finally, the combination of the acceleration of the flow due to the throat restriction and the reduced recirculation flow produce an increased swirl transfer and α angle, which produce in this case a lower β angle and incidence, improving the flow attachment in the suction face of the blades and thus, the stability increases. Again, in spite of being interesting parameters of the behavior of the flow at the compressor inlet, these angles cannot be taken independently as unique indicators of the closeness of the surge limit.

The reach of the recirculation and its impact on the incoming flow may also be graphically analyzed thanks to the longitudinal sections shown in Fig. 5. In these figures, combinations of linear integral convolutions [43] of the

time-averaged velocity are used with the mean temperature in the color field. In addition, average velocity vectors and a null axial velocity line are added to the figures, highlighting backflow region. The location of the inducer plane is marked in each geometry.

The solutions of the reference case and the tapered duct are shown in Figs. 5a and 5b, where the backflows freely traveling upstream can be seen, transferring swirl and enthalpy to the incoming flow. Notice the non-axisymmetry of the time-averaged flow, particularly at the tapered duct (Fig. 5b). This is due to the non-axisymmetric shape of the volute. On the other side, in Figs. 5c and 5d it can be observed how the nozzles confine this region, limiting that transfer. As aforementioned, higher confinement of the backflows implies lower meridional momentum transfer and thus, a different velocity triangle configuration.

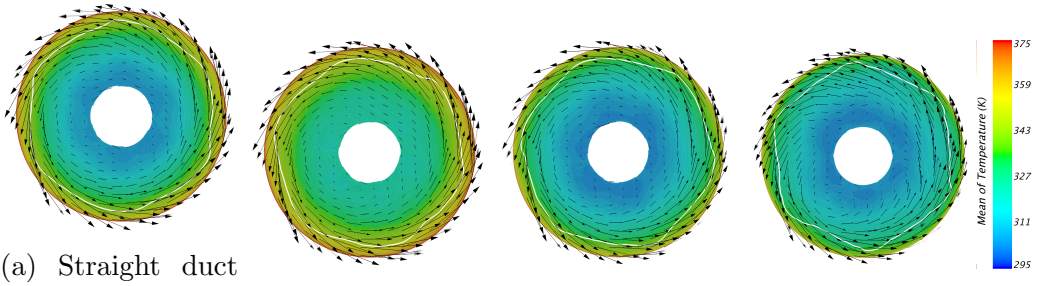

(a) Straight duct (baseline) (b) Tapered duct (c) C-D nozzle (d) Convergent nozzle

Figure 6: Inducer cross-section of linear integral convolution of mean velocity, scalar of mean temperature, mean velocity vectors and white solid line indicates null axial velocity for the low mass flow rates simulations.

The same variables used in Fig. 5 are depicted in Fig. 6 on the inducer plane sections of all the configurations, seeking an understanding of secondary flows. However, the pre-rotation of the flow (high α values in Table 4) produced by the tangential momentum transfer from the backflows to the incoming flow dominates over other secondary flows. Higher temperatures can be seen in the inducer plane of the tapered configuration (6b), not only across the incoming boundary but also the backflows are hotter compared with the results of the nozzles. The explanation resides in the backflows that start in a region where the gas is partially compressed and heated, implying that the higher the incoming temperature the higher the temperature of the outgoing backflows, what increases, additionally, the incoming flow temper-

ature. This is a problem that feeds itself back and produces an amplified solution, which should be considered for the selection of materials that can bear such temperatures. On the other side, the velocity vectors and the backflow contour delimitation is similar across all the configurations.

A different approach to analyze the momentum distribution may be done performing a meridional averaging of the axial momentum parameter, as seen in Fig. 7. The solid line indicates the region of null meridional averaged momentum, and thus null meridional averaged velocity.

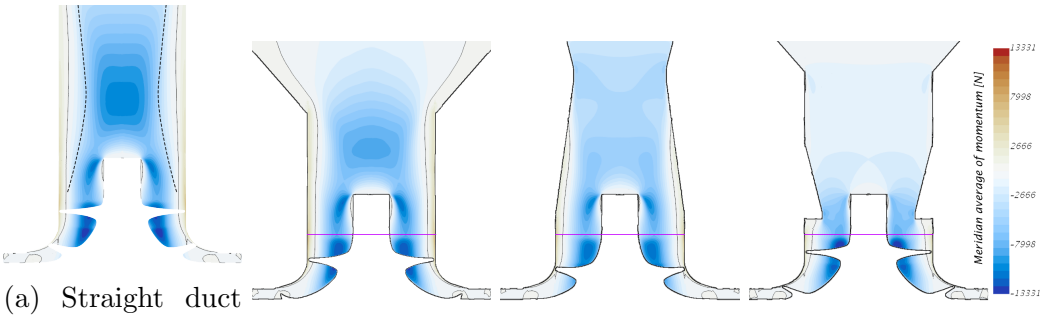

(a) Straight duct (baseline) (b) Tapered duct (c) C-D nozzle (d) Convergent nozzle

Figure 7: Axial section of meridian average of momentum and line of null momentum.

First, a local maximums of axial velocity are found upstream the impeller nut for the straight and tapered ducts. Incoming velocity contours show a C-D nozzle-like pattern due to the backflows. This effect is more clear for the straight duct (see dashed line, made just for remarking this effect). In fact, the divergent part of this "nozzle" may reach an angle that the flow cannot withstand without detachment with lower mass flow rate. Contradictorily, the acceleration of the flow in the throat and thus, the momentum on the inducer plane, is lower for the C-D nozzle. This is due to the lower room occupied by the backflows in the latter configuration which in the end sets the effective throat. Finally, the acceleration produced in the convergent nozzle is moved downstream, closer to the impeller and reducing the deflection produced by the nut. Again, due to the confinement of the backflows the momentum in the inducer plane is lower than the baseline, as already seen in Table 3.

Regarding the global variables obtained for the points of low mass flow rate, Equations 1 and 2 are used to calculate the compression ratio and the isentropic efficiency and showed in Table 5. The average incoming temperature in the inducer plane of each intake geometry is written as well.

	Str.	**Tap.**	**CD-N**	**C-N**
$\Pi_{t,t}$	2.12	2.11	2.13	2.15
η_s	56.3	56.1	58.5	59.2
T_{ind} [°C]	46.3	49.1	41.6	39.1

Table 5: Results of compression ratio, efficiency and average incoming temperature for the low mass flow rate points.

Higher efficiencies are found for both nozzles, which correlates with lower recirculation ratios, as seen in Table 3. Moreover, considering the values of incoming temperature, it can be concluded that confining the backflows reduces their interaction with the incoming flow and thus, friction losses decrease as well, what translates into an isentropic efficiency rise. However, it is worth noticing that the different friction losses are not the only responsible of different efficiencies, an alteration of the flow pattern on the inducer may also affect the resulting efficiency, as a different compressor trim would do. Conversely, similar results of momentum and recirculation between the tapered duct and the baseline straight duct also produce similar friction losses and thus, efficiencies. The compression ratio is marginally influenced by any intake geometry.

The efficiency rise obtained for both nozzles at low mass flow rate cannot be directly extrapolated to different regions of the compressor map, since the flow structures would be quite different. Nevertheless, previously, Desantes et al. [13] and Galindo et al. [24] tested a similar C-D nozzle obtaining an efficiency increase not only at points close to surge also at mid mass flow rates, even increasing by 6 percentage points the maximum efficiency of the compressor.

Concerning the noise assessment, the PSD is calculated using the Method of Characteristics wave decomposition defined in Eq. 3 and the Welch's averaging introduced in section 3. Figure 8 shows the PSD results at the inlet and outlet ducts.

It is noticeable that each case presents a different PSD profile for frequencies between 800 and 2500 Hz, coinciding with the common range of the *whoosh* noise [5, 44, 45]. Nevertheless, except the straight duct, that presents a flat and noisy spectra at very-low frequencies, the rest of the configurations show a noticeable peak in the aforementioned whoosh noise range possibly responsible of this characteristic noise. Also, all PSD show an important peak at very low frequencies, nearly about 100 Hz or RO=0.04, which ac-

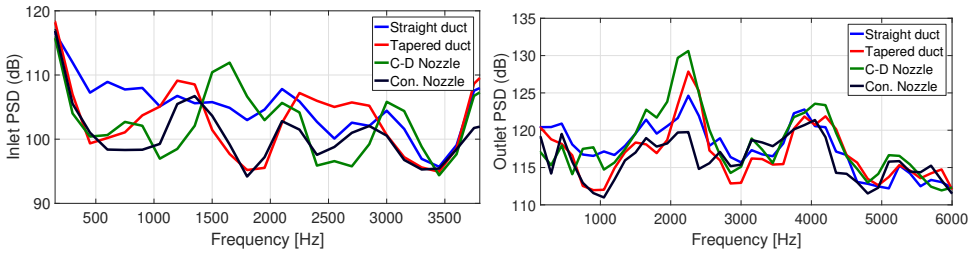

(a) Inlet PSD (b) Outlet PSD

Figure 8: Inlet and outlet PSD of low mass flow rate points.

cording to Sundström et al. [42] is due to the dominant surge oscillation. Using Equations 5 and 6, the SIL are computed and the results are shown in Table 6. It can be seen that, in average, the straight duct produces a significantly higher noise emission, which according to Evans et al. [5], may suggest that the compressor is operating very close to surge, as would be consistent with the experimental campaign.

SIL (dB)	**Str.**	**Tap.**	**CD-N**	**C-N**
Inlet	131	126	126	122
Outlet	151	152	154	149

Table 6: Inlet and outlet SIL of low mass flow rate points in a frequency window from 300 to corresponding cut-off frequency.

Broatch et al. [36] stated that the *whoosh* noise is affected by inducer rotating stall, which in turn, can be enhanced by the onset of low-pressure bubbles that appear at low mass flow rates [22]. In Fig. 9 the low-pressure bubbles at the straight inlet duct are shown, displaying the region whose pressure is below 90 kPa. The bubbles rotate in the same direction as the wheel, due to the angular momentum transfer from the recirculations to the intake mass flow, but at a lower speed rate. The rotating speed was assessed and resulted to be spinning nearly at RO=0.5, this is, at around 1333 Hz, which coincide with the aforementioned peaks found within the *whoosh* noise range [46]. Conversely, from 3500 Hz to higher frequencies, the inlet geometry appears to have no impact on the PSD, except for the convergent nozzle. The PSD spectra profile of this geometry is strongly modified due to the partial blockage of the inducer area. Actually, the convergent nozzle case produce, in average, a lower noise emission (see table 6). The experimental tests carried

out by Galindo et al. [24] showed a lower SIL emission of the convergent nozzle inlet as well.

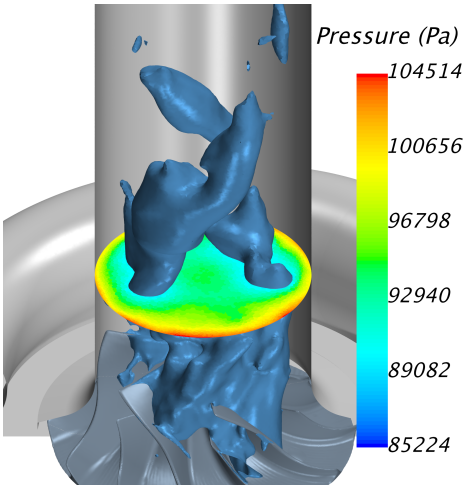

Figure 9: Low-pressure bubble at low mass flow rates for the straight duct.

Although the outlet duct does not directly discharge to the ambient, the analysis of its spectra is important since the intensity of the noise is greater than at the inlet ([5], Table 6) and therefore the compressor housing and outlet pipe may significantly radiate noise to the surroundings, as described by Torregrosa et al. [47]. Additionally, being that the engine is placed downstream of the compressor and it is greatly influenced by the acoustic signature of its intake flow, special attention needs to be paid when coupling both thermal machines. Figure 11b shows the PSD of the outlet ducts, where a similar spectral profile is generated by all four configurations, differing only in the power density of the peaks around 2200 Hz. Analogously to the inlet PSD, the convergent nozzle case produce the lower peak, whereas the tapered and the C-D nozzle cases produce higher values.

4.2. Points of high mass flow rate

At high mass flow rates, the effect of the inlet geometry is clear on the evolution of the static pressure through the intake duct, since the pressure losses grow with the square of the mass flow rate. Moreover, flow recirculation is not extended upstream the impeller at these conditions [32] because the higher mass flow rate implies a greater momentum that is able to overcome the adverse pressure gradient set in the rotor easier, therefore creating

backflows of lower intensity than near surge (see Fig. 7. The impact of the shifting the operating point in the angles of velocity triangle (according to the definition in Fig. 4) is shown in Table 7.

Angle [°]	**Str.**	**Tap.**	**CD-N**	**C-N**
α	0.2	0.2	1.1	4.0
β	50.1	49.9	44.9	32.9
i	3.1	2.9	-2.1	-14.1

Table 7: Alpha and beta angles for the high mass flow cases.

Angles for high mass flow rate (100 g/s) included in Table 7 present significant differences to their counterparts at 30 g/s, shown in Table 4. First, c_u component is reduced because the recirculation intensity decreases, as commented before. This entails a reduction in the swirl transfer with the incoming flow, which is kept almost axial until entering the compressor inducer, producing α values close to zero. In the case of the Convergent nozzle, the presence of the throat near of the inducer generates a sudden expansion. This "backward facing step" for the incoming flow results in flow detachment, promoting recirculation in the fashion of a rotating bubble that covers the backside of the step and the inducer region close to the shroud, as can be seen in Fig. 10. Great swirl transfer is produced there, slightly increasing c_u component and thus the averaged alpha angle of the Convergent nozzle in Table 7.

Besides, the higher axial velocity component compared with the low mass flow rate points also contributes to reducing α and β values, according to Fig. 4. Notice the shift from positive incidence in Table 4 to close-to-zero incidence in Table 7 due to the combination of the aforementioned factors.

When the cross-section of the incoming flow is reduced, which happens with both nozzles, axial velocity is even higher, which further reduces β and i. The throat created by the Convergent nozzle decreases the incidence angle down to -14° and generates the pressure losses that strongly worsens the compressor efficiency. The results of the global variables for the high mass flow rates are written in Table 8.

The higher pressure losses of the Convergent nozzles worsen both the compression ratio and the efficiency. A different point of view to approach this would be assessing the Mach number at the inducer plane. In Fig. 10 it can be seen how the Mach number reaches supersonic velocities in some

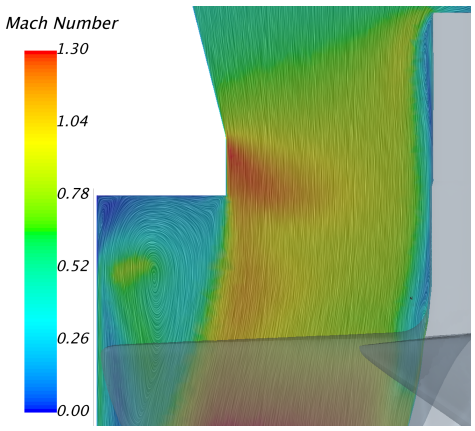

Figure 10: LIC of mean absolute velocity with color field of Mach number of convergent nozzle at high mass flow rates.

	Str.	**Tap.**	**CD-N**	**C-N**
$\Pi_{t,t}$	1.65	1.64	1.56	1.11
η_s	63.0	62.3	55.1	14.1

Table 8: Results of compression ration and efficiency for the high mass flow rate points.

regions of the impeller. First, the throat appears to be partially blocked and even producing supersonic flows. The presence of shock waves and supersonic flow imply important losses of the total conditions, responsible of the efficiency decrease. The same effect would be found for the rest of the configurations at higher mass flow rates or at the same conditions with a smaller compressor (or with a compressor with a lower trim). It is worth mentioning that this effect is also noticeable with the C-D nozzle, but not as importantly. On the contrary, the tapered duct does not have any worse or better influence on the compression ratio or on the efficiency compared with the straight duct.

Finally, regarding the noise analysis of the high mass flow rate points, again the Method of Characteristics wave decomposition (Eq. 3) and the Welch's averaging is used to calculate the PSD. In Fig. 11 is depicted the PSD results at the inlet and outlet ducts. The PSD of these points is lower compared with the corresponding low mass flow rate ones, which is consistent with the experimental results obtained by Galindo et al. [24] and the simulations performed by Broatch et al. [22] and Sundström et al. [48]. The impact of the sonic conditions of the flow in the throat of the Convergent nozzle (see

Fig. 10) is noticeable. Due to the flow being supersonic, the noise generated downstream the throat, i.e., in the compressor wheel, diffuser, volute and outlet duct, cannot travel upstream and reach the inlet entry. Since the rotor is the source the loudest noise of the system, the PSD at the inlet duct is significantly reduced. The rest of the configurations present a flatter noise signature, again being the straight duct the flattest. The peaks of the C-N nozzle points towards some degree of acoustic resonance that is related to the specific geometry that has been employed. The PSD of the outlet duct is less critical, however it is interesting how both nozzles present a higher noise level from 3000 Hz on. This should be considered for the engine gas exchange design and the radiated noise [47].

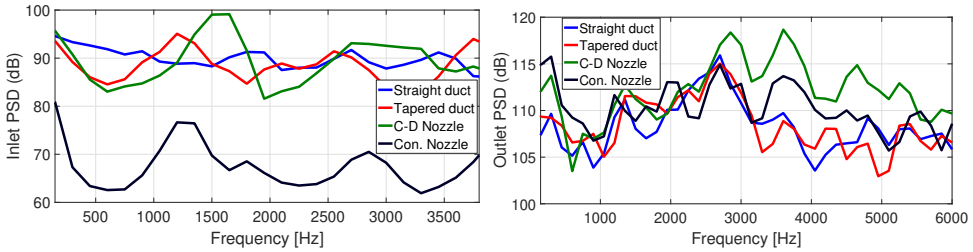

(a) Inlet PSD (b) Outlet PSD

Figure 11: Inlet and outlet PSD of high mass flow rate points.

The SIL has been calculated as well using Eqs. 5 and 6, and the results are exposed in Table 9. The results of the straight duct and the nozzles are consistent with the experimental data obtained by Galindo et al. [24]. However the Tapered configuration presents a lower SIL than in the experimental test. This may be due to its geometrical characterization (different compressor design, length of the ducts, similar but not identical diameters, ...), which greatly affects noise signature and resonances.

SIL (dB)	**Str.**	**Tap.**	**CD-N**	**C-N**
Inlet	123	113	115	87
Outlet	147	148	152	148

Table 9: Inlet and outlet SIL of high mass flow rate points in a frequency window from 300 to corresponding cut-off frequency.

5. Conclusions

Four compressor inlet geometries were selected and modeled. Compressor simulations with these geometries were made setting two operating points, one close to surge at 30 g/s and one at very high mass flow rates at 100 g/s, both at the same compressor speed of 160 krpm. From the converged simulations, global variables were obtained, local observations in different section planes were assessed and the noise emission produced in both inlet and outlet ducts were measured, using the Method of Characteristics for the wave decomposition.

From the results of each intake geometry in comparison to the baseline at low mass flow rate can be extracted that:

- Tapered duct: similar results are obtained in all the quantitative parameters that has been assessed (recirculation, incidence angle, global variables, etc), in both low and high mass flow rates. The effective "nozzle" that appears when the recirculation constraints the incoming flow is less visible than in the straight duct, possibly influencing on the surge limit.

- Convergent-Divergent nozzle: less incoming momentum and recirculation values resulted from the simulation, but the lower interaction with the backflows reduced the enthalpy transfer and the friction losses, which implied a colder incoming flow and an increased compressor efficiency. The area restriction of the throat worsens the performance at high mass flow rates.

- Convergent nozzle: the effects found in the C-D nozzle are aggravated with this intake geometry. Nevertheless, in spite of having the lowest recirculation and momentum values, the swirl at the inducer plane produces the highest α and incidence values, increasing the stability at low mass flow rates. The incoming temperature is lower as well, producing an increase in efficiency. Drawbacks of this configuration appear when the mass flow rate increases and the pressure losses of the cross-section restriction counter-acts the aforementioned benefits.

Finally, concerning the noise analysis, it is concluded that the inlet geometry plays an important role on the characterization of the emitted spectra at low mass flow rates, not only setting the global intensity but also altering the noise signature, potentially impacting in the subjective perception of

the complete engine noise, aspect that has grown in importance in the latter years. The outlet pressure waves are also influenced by the inlet geometry, so its study cannot be discarded beforehand for modeling the acoustic response of the whole gas exchange process of the engine. A slight noise reduction is found for the tapered and C-D nozzle and a significant reduction is produced by the convergent nozzle due to the partial blockage of the inlet area, particularly at high mass flow rates.

For future works, the simulation of even lower mass flow rate points is proposed, with the objective of both determining if the prediction of surge onset provided by CFD simulations correspond with the experimental tests carried out using the same inlet geometries and assessing the phenomena responsible of its triggering.

6. Acknowledgements

Daniel Tarí is partially supported through contract FPI-S2-2015-1095 of Programa de Apoyo para la Investigación y Desarrollo (PAID) of Universitat Politècnica de València.

References

[1] J. M. Luján, H. Climent, L. M. García-Cuevas, A. Moratal, Pollutant emissions and diesel oxidation catalyst performance at low ambient temperatures in transient load conditions, Applied Thermal Engineering 129 (2018) 1527 – 1537. doi:10.1016/j.applthermaleng.2017.10.138.

[2] M. Wei, S. Li, H. Xiao, G. Guo, Combustion performance and pollutant emissions analysis using diesel/gasoline/iso-butanol blends in a diesel engine, Energy Conversion and Management 149 (2017) 381 – 391. doi:10.1016/j.enconman.2017.07.038.

[3] K. Ekberg, L. Eriksson, Improving Fuel Economy and Acceleration by Electric Turbocharger Control for Heavy Duty Long Haulage, IFAC-PapersOnLine 50 (1) (2017) 11052 – 11057, 20th IFAC World Congress. doi:10.1016/j.ifacol.2017.08.2486.

[4] A. Romagnoli, W.-I. Wan-Salim, B. Gurunathan, R. Martinez-Botas, J. Turner, N. Luard, R. Jackson, L. Matteucci, C. Copeland, S. Akehurst, A. Lewis, C. Brace, Assessment of supercharging boosting com-

List of Symbols

a	speed of sound	$m \cdot s^{-1}$
c_p	isobaric specific heat capacity	$J \cdot kg^{-1} \cdot K^{-1}$
c	absolute velocity	$m \cdot s^{-1}$
I	sound intensity	$W \cdot m^{-2}$
i	incidence angle	$^\circ$
M	Mach number	$-$
N	compressor rotational speed	rpm
p	pressure	Pa
r	radial coordinate	m
T	temperature	K
u	blade linear velocity	$m \cdot s^{-1}$
W	compressor specific work	$J \cdot kg^{-1}$
w	relative velocity	$m \cdot s^{-1}$
α	absolute flow angle	$^\circ$
β	relative flow angle	$^\circ$
η	compressor efficiency	%
γ	ratio of specific heats	$-$
$\Pi_{t,t}$	total-to-total pressure ratio	$-$
ρ	density	$kg \cdot m^{-3}$
ω	rotational speed	$rad \cdot s^{-1}$

Sub- and Superscripts

0	mean variable
a	axial component
$back$	backward travelling wave
ind	inducer
in	inlet duct
$forw$	forward travelling wave
$l.e.$	leading edge
out	outlet duct
s	isentropic
ref	reference value
t	stagnation variable
u	tangential component

ponent for heavily downsized gasoline engines , in: I. o. M. Engi-

List of abbreviations and acronyms

3D	three dimensional
CAD	computer-aided design
C, Conv	convergent
C-D	convergent-divergent
CFD	computational fluid dynamics
IGV	inlet guide vanes
LDV	laser doppler velocimetry
LIC	line integral convolution
MoC	Method of Characteristics
PIV	particle image velocimetry
PSD	power spectral density
RO	rotating order
SIL	sound intensity level
Str.	straight
Tap.	tapered

neers (Ed.), 11th International Conference on Turbochargers and Turbocharging, Woodhead Publishing, Oxford, 2014, pp. 13 – 26. doi:10.1533/978081000342.13.

[5] D. Evans, A. Ward, The reduction of turbocharger whoosh noise, in: 8^{th} International Conference on Turbochargers and Turbocharging, IMechE, 2006.

[6] J. Galindo, J. R. Serrano, C. Guardiola, C. Cervelló, Surge limit definition in a specific test bench for the characterization of automotive turbochargers, Experimental Thermal and Fluid Science 30 (5) (2006) 449–462. doi:10.1016/j.expthermflusci.2005.06.002.

[7] X. Zheng, Z. Sun, T. Kawakubo, H. Tamaki, Experimental investigation of surge and stall in a turbocharger centrifugal compressor with a vaned diffuser, Experimental Thermal and Fluid Science 82 (2017) 493 – 506. doi:10.1016/j.expthermflusci.2016.11.036.

[8] A. Epstein, J. Ffowcs Williams, E. Greitzer, Active suppression of aerodynamic instabilities in turbomachines, Journal of Propulsion and Power 5 (2) (1989) 204–211. doi:10.2514/3.23137.

[9] M. Zhang, X. Zheng, Criteria for the matching of inlet and outlet distortions in centrifugal compressors, Applied Thermal Engineering 131 (2018) 933 – 946. doi:10.1016/j.applthermaleng.2017.11.140.

[10] J. Galindo, J. R. Serrano, X. Margot, A. Tiseira, N. Schorn, H. Kindl, Potential of flow pre-whirl at the compressor inlet of automotive engine turbochargers to enlarge surge margin and overcome packaging limitations, International journal of heat and fluid flow 28 (3) (2007) 374–387. doi:10.1016/j.ijheatfluidflow.2006.06.002.

[11] B. Zhao, H. Sun, L. Wang, M. Song, Impact of inlet distortion on turbocharger compressor stage performance, Applied Thermal Engineering 124 (2017) 393 – 402. doi:10.1016/j.applthermaleng.2017.05.181.

[12] A. Engeda, Y. Kim, R. Aungier, G. Direnzi, The inlet flow structure of a centrifugal compressor stage and its influence on the compressor performance, Journal of fluids engineering 125 (5) (2003) 779–785. doi:10.1115/1.1601255.

[13] J. Desantes, J. M. Luján, B. Pla, J. Soler, Potential of using a nozzle at the compressor inlet of a high-speed direct-injection diesel engine, Proceedings of the Institution of Mechanical Engineers, Part D: Journal of Automobile Engineering 225 (2) (2011) 178–189. doi:10.1243/09544070JAUTO1429.

[14] S. Sharma, M. Jupp, S. Barrans, K. Nickson, The impact of housing features relative location on a turbocharger compressor flow, International Journal of Mechanical Engineering and Robotics Research 6 (6) (2017) 451–457.

[15] Y. Mingyang, R. Martinez-Botas, D. Kangyao, Z. Yangjun, Z. Xinqian, Unsteady influence of Self Recirculation Casing Treatment (SRCT) on high pressure ratio centrifugal compressor, International Journal of Heat and Fluid Flow 58 (2016) 19 – 29. doi:10.1016/j.ijheatfluidflow.2015.12.004.

[16] B. Semlitsch, M. Mihaescu, Flow phenomena leading to surge in a centrifugal compressor , Energy 103 (2016) 572 – 587. doi:10.1016/j.energy.2016.03.032.

[17] I. Tomita, B. An, T. Nanbu, A new operating range enhancement device combined with a casing treatment and inlet guide vanes for centrifugal compressors, in: I. o. M. Engineers (Ed.), 11th International Conference on Turbochargers and Turbocharging, Woodhead Publishing, Oxford, 2014, pp. 79 – 87. doi:10.1533/978081000342.79.

[18] G. Capon, T. Morris, The effect of air inlet system features on automotive turbocharger compressor performance, in: 9^{th} International Conference on Turbochargers and Turbocharging, 2010.

[19] O. Baris, F. Mendonça, Automotive Turbocharger Compressor CFD and Extension Towards Incorporating Installation Effects, in: Proceedings of ASME Turbo Expo 2011: Power for Land, Sea and Air, ASME, 2011, pp. 2197–2206. doi:10.1115/GT2011-46796.

[20] R. P. Tanna, J. Yin, B. Sirakov, V. Barbarie, Development of ported shroud compressor housing with reduced compressor blade pass source acoustic level, in: 9^{th} International Conference on Turbochargers and Turbocharging, 2010.

[21] N. Figurella, R. Dehner, A. Selamet, K. Tallio, K. Miazgowicz, R. Wade, Noise at the mid to high flow range of a turbocharger compressor, in: 41^{st} International Congress and Exposition on Noise Control Engineering 2012, Vol. 2012, Institute of Noise Control Engineering, 2012, pp. 786–797.
URL http://www.ingentaconnect.com/content/ince/incecp/2012/00002012/00000003/art00015

[22] A. Broatch, J. Galindo, R. Navarro, J. García-Tíscar, Numerical and experimental analysis of automotive turbocharger compressor aeroacoustics at different operating conditions, International Journal of Heat and Fluid Flow 61 (2016) 245 – 255. doi:10.1016/j.ijheatfluidflow.2016.04.003.

[23] K.-K. Ha, T.-B. Jeong, S.-H. Kang, H.-J. Kim, K.-M. Won, C.-Y. Park, W.-Y. Jung, K.-S. Cho, Experimental investigation on aero-acoustic characteristics of a centrifugal compressor for the fuel-cell vehicle, Journal of Mechanical Science and Technology 27 (11) (2013) 3287–3297. doi:10.1007/s12206-013-0851-y.

[24] J. Galindo, A. Tiseira, R. Navarro, D. Tarí, C. M. Meano, Effect of the inlet geometry on performance, surge margin and noise emission of an automotive turbocharger compressor, Applied Thermal Engineering 110 (2017) 875–882. doi:10.1016/j.applthermaleng.2016.08.099.

[25] E. Guillou, M. Gancedo, E. Gutmark, A. Mohamed, PIV investigation of the flow induced by a passive surge control method in a radial compressor, Experiments in fluids 53 (3) (2012) 619–635. doi:10.1007/s00348-012-1310-8.

[26] S.-B. Ma, K.-Y. Kim, Optimization of discrete cavities in a centrifugal compressor to enhance operating stability, Aerospace Science and Technology 68 (2017) 308 – 319. doi:10.1016/j.ast.2017.05.029.

[27] A. Broatch, J. Galindo, R. Navarro, J. García-Tíscar, Methodology for experimental validation of a CFD model for predicting noise generation in centrifugal compressors, International Journal of Heat and Fluid Flow 50 (2014) 134–144. doi:10.1016/j.ijheatfluidflow.2014.06.006.

[28] F. Mendonça, O. Baris, G. Capon, Simulation of Radial Compressor Aeroacoustics using CFD, in: Proceedings of ASME Turbo Expo 2012, no. GT2012-70028, ASME, 2012, pp. 1823–1832. doi:10.1115/GT2012-70028.

[29] CD-adapco, STAR-CCM+, release version 11.06.010 Edition (2016). URL http://www.cd-adapco.com

[30] R. Lang, Contribución a la Mejora del Margen de Bombeo en Compresores Centrífugos de Sobrealimentación, Ph.D. thesis, Universitat Politècnica de València (2011).

[31] J. Galindo, A. Tiseira, R. Navarro, M. López, Influence of tip clearance on flow behavior and noise generation of centrifugal compressors in near-surge conditions, International Journal of Heat and Fluid Flow 52 (2015) 129–139. doi:10.1016/j.ijheatfluidflow.2014.12.004.

[32] R. Navarro, Predicting Flow-Induced Acoustics at Near-Stall Conditions in an Automotive Turbocharger Compressor: A Numerical Approach, Springer, 2018. doi:10.1007/978-3-319-72248-1.

[33] A. Travin, M. Shur, M. Strelets, P. Spalart, Detached-eddy simulations past a circular cylinder, Flow, Turbulence and Combustion 63 (1-4) (2000) 293–313.

[34] S. Fontanesi, S. Paltrinieri, G. Cantore, CFD Analysis of the Acoustic Behavior of a Centrifugal Compressor for High Performance Engine Application, Energy Procedia 45 (0) (2014) 759–768, aTI 2013 - 68th Conference of the Italian Thermal Machines Engineering Association. doi:10.1016/j.egypro.2014.01.081.

[35] R. van Rennings, K. Shi, S. Fu, F. Thiele, Delayed-Detached-Eddy Simulation of Near-Stall Axial Compressor Flow with Varying Passage Numbers, in: S. Fu, W. Haase, S.-H. Peng, D. Schwamborn (Eds.), Progress in Hybrid RANS-LES Modelling, Vol. 117 of Notes on Numerical Fluid Mechanics and Multidisciplinary Design, Springer Berlin Heidelberg, 2012, pp. 439–448. doi:10.1007/978-3-642-31818-4_38.

[36] A. Broatch, J. Galindo, R. Navarro, J. García-Tíscar, A. Daglish, R. K. Sharma, Simulations and measurements of automotive turbocharger compressor whoosh noise, Engineering Applications of Computational Fluid Mechanics 9 (1). doi:10.1080/19942060.2015.1004788.

[37] A. J. Torregrosa, P. Fajardo, A. Gil, R. Navarro, Development of a non-reflecting boundary condition for application in 3D computational fluid dynamic codes, Engineering Applications of Computational Fluid Mechanics 6 (3) (2012) 447–460. doi:10.1080/19942060.2012.11015434.

[38] L. J. Eriksson, Higher order mode effects in circular ducts and expansion chambers, The Journal of the Acoustical Society of America 68 (1980) 545. doi:10.1121/1.384768.

[39] P. Welch, The use of fast fourier transform for the estimation of power spectra: a method based on time averaging over short, modified periodograms, Audio and Electroacoustics, IEEE Transactions on 15 (2) (1967) 70–73.

[40] K. Holland, P. Davies, The measurement of sound power flux in flow ducts, Journal of Sound and Vibration 230 (4) (2000) 915–932. doi:10.1006/jsvi.1999.2656.

[41] J. Galindo, F. Arnau, A. Tiseira, R. Lang, H. Lahjaily, T. Gimenes, Measurement and modeling of compressor surge on engine test bench for different intake line configurations, SAE Technical Paper 2011-01-0370. doi:10.4271/2011-01-0370.

[42] E. Sundström, B. Semlitsch, M. Mihăescu, Generation Mechanisms of Rotating Stall and Surge in Centrifugal Compressors, Flow, Turbulence and Combustion 100 (3) (2018) 705–719. doi:10.1007/s10494-017-9877-z.

[43] B. Cabral, L. C. Leedom, Imaging vector fields using line integral convolution, in: Proceedings of the 20^{th} annual conference on Computer graphics and interactive techniques, ACM, 1993, pp. 263–270. doi:10.1145/166117.166151.

[44] E. P. Trochon, A new type of silencers for turbocharger noise control, SAE Technical Paper 110 (6) (2001) 1587–1592. doi:10.4271/2001-01-1436.

[45] G. Gaudé, T. Lefèvre, R. Tanna, K. Jin, T. J. B. McKitterick, S. Armenio, Experimental and computational challenges in the quantification of turbocharger vibro-acoustic sources, in: Proceedings of the 37^{th} International Congress and Exposition on Noise Control Engineering 2008, Vol. 2008, Institute of Noise Control Engineering, 2008, pp. 5598–5611.

[46] R. Kabral, M. Abom, Investigation of turbocharger compressor surge inception by means of an acoustic two-port model, Journal of Sound and Vibration 412 (2018) 270–286. doi:10.1016/j.jsv.2017.10.003.

[47] A. J. Torregrosa, A. Broatch, R. Navarro, J. García-Tíscar, Acoustic characterization of automotive turbocompressors, International Journal of Engine Research 16 (1) (2015) 31–37. doi:10.1177/1468087414562866.

[48] E. Sundström, B. Semlitsch, M. Mihăescu, Acoustic signature of flow instabilities in radial compressors, Journal of Sound and Vibration 434 (2018) 221 – 236. doi:https://doi.org/10.1016/j.jsv.2018.07.040.
URL http://www.sciencedirect.com/science/article/pii/S0022460X1830484X